Nanoscale Integrin Ligand Patterns Determine Melanoma Cell Behavior

Katharina Amschler,[†] Luise Erpenbeck,[†] Sebastian Kruss,[‡] and Michael P. Schön[†,*]

[†]Department of Dermatology, Venereology and Allergology, Georg August University, Göttingen, Germany and [‡]Max Planck Institute for Intelligent Systems, Stuttgart, Germany

ABSTRACT Cells use integrin receptors to adhere onto surfaces by binding to ligands such as the arginine-glycine-aspartic acid (RGD) motif. Cancer cells make use of this adhesion process, which has motivated the development of integrin-directed drugs. However, those drugs may exert paradoxical effects on tumor progression, which raises the question of how integrin function is governed in tumor cells on the nanoscale. We have utilized precisely defined and tunable RGD ligand site densities spanning 1 order of magnitude, *i.e.*, 103 to 1145 ligand sites/μm^2, by using RGD-functionalized gold nanoparticle patterns immobilized on glass by block copolymer (micellar) nanolithography. In an $\alpha_V\beta_3$ integrin-dependent fashion, human melanoma cells spread, formed focal contacts, and reorganized cytoskeletal fibers on a physiologically relevant RGD density of 349 sites/μm^2. Intriguingly, low doses of solute RGD "shifted" the optimal densities of immobilized ligand along with corresponding melanoma cell integrin clusters and cytoskeletal changes toward those typical for "intermediate" ligand presentation. Consequently, melanoma cells were forced into a "permissive" state, optimizing interactions with suboptimal nanostructured biomimetic surfaces, thus providing an explanation for the seemingly paradoxical effects on tumor progression and a potential clue for individualized antitumoral therapies.

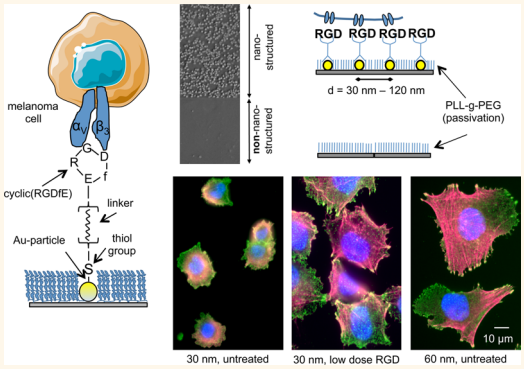

KEYWORDS: melanoma · cell spreading · RGD · nanostructures · integrin · ligand presentation

Notwithstanding recent therapeutic advances including immune modulation or inhibition of mutated BRAF,[1,2] metastasized melanoma is usually fatal within a few months. Melanoma cells adapt flexibly to the tumor (micro)environment within distant organs and can switch from sessile to spreading phenotypes by "abusing" the surrounding tissue. The latter interactions are mediated primarily by integrins binding to recognition motifs within the extracellular matrix (ECM).[3−5]

The $\alpha_V\beta_3$ integrin is an instructive example of a receptor that is strongly up-regulated on melanoma cells and tumor-associated blood vessels.[6,7] It is, therefore, conceivable that blocking this receptor will interfere with melanoma progression. Indeed, the $\alpha_V\beta_3$/$\alpha_V\beta_5$-blocking arginine-glycine-aspartic acid (RGD) analogue cilengitide has been tested in clinical trials for treating solid tumors.[8−10] Although preclinical studies have demonstrated good efficacy against melanoma cells,[11,12] a recent clinical phase II trial has met with limited success.[13] While such discrepancies between promising preclinical observations and sobering clinical results are not unusual in the field of melanoma therapy, there is an interesting twist in the case of cilengitide-treated melanoma inasmuch as low doses of RGD analogues "paradoxically" enhanced tumor growth.[14] However, the mechanistic basis of this intriguing observation remains largely speculative.[14,15]

Although integrins and their ligands have been studied intensively in the context of melanoma progression,[16−18] most studies have neglected important physiological characteristics of ligand presentation. Indeed, migration and spreading appear to be regulated not only by ligand specificity but also by biophysical properties such as density and spatial orientation,[19−22] thus highlighting the relevance of studying receptor−ligand interactions on a nanoscopical, preferably even single-molecule, level.

In order to assess subcellular responses of human melanoma cells to crucial extracellular ligands, a function that has been implicated in tumor progression and

* Address correspondence to michael.schoen@med.uni-goettingen.de.

Received for review May 16, 2014 and accepted August 29, 2014.

Published online August 29, 2014
10.1021/nn502690b

targeted therapies, we have used a modified block copolymer (micellar) nanolithography (BCML) method[23−27] that features nanostructured surfaces with defined interparticle spacings ranging from 30 to 120 nm (corresponding to receptor site densities from 1145 to 103/μm^2) to present the integrin recognition motif RGD (R = arginine, G = glycine, D = aspartic acid) in a proper orientation. We chose the pentapeptide cyclic(RGDfE) for functionalization because it showed preferential binding to the $\alpha_V\beta_3$ integrin.[28,29]

We demonstrate that $\alpha_V\beta_3$-expressing melanoma cells spread best on "intermediate" RGD site densities, while mere adhesion was linearly dependent on ligand density. Tuning the RGD nanopatterns in either direction conspicuously attenuated tumor cell spreading, focal contact formation, and cytoskeletal reorganization. Blocking peptides at less-than-optimal dosages "shifted" the optimal ligand densities together with the corresponding melanoma cell behavior toward a "permissive" receptor−ligand ratio. Thus, our results provide unexpected insights into the complex regulation of cell morphogenesis in response to defined ligand engagement and thus contribute to understanding seemingly "paradoxical" tumor cell responses.

RESULTS

Nanostructured RGD Surfaces Exhibit Precisely Defined Densities and Facilitate Melanoma Cell Binding. RGD is a crucial ECM recognition motif. Using block copolymer (micellar) nanolithography to control density and lateral spacing of gold nanoparticles (Au-NPs) on glass surfaces, we generated bioinspired surfaces by functionalization of Au-NPs with cyclic(RGDfE), a pentapeptide specific for the $\alpha_V\beta_3$ integrin (Figure 1A−C).[28,29] These Au-NP patterns exhibit precisely defined densities with a *quasi*-hexagonal configuration, and the spacings between the nanoparticles can be adjusted.[24] On the basis of steric considerations it can be reasonably assumed that one Au-NP represents a single integrin-binding site.[24]

We generated Au-NP patterns ranging from 30 to 120 nm (Figure 1A). As determined by SEM analyses, these patterns corresponded to ligand site densities of 1145/μm^2 to 103/μm^2, thus spanning 1 order of magnitude. Moreover, these surfaces covered RGD site

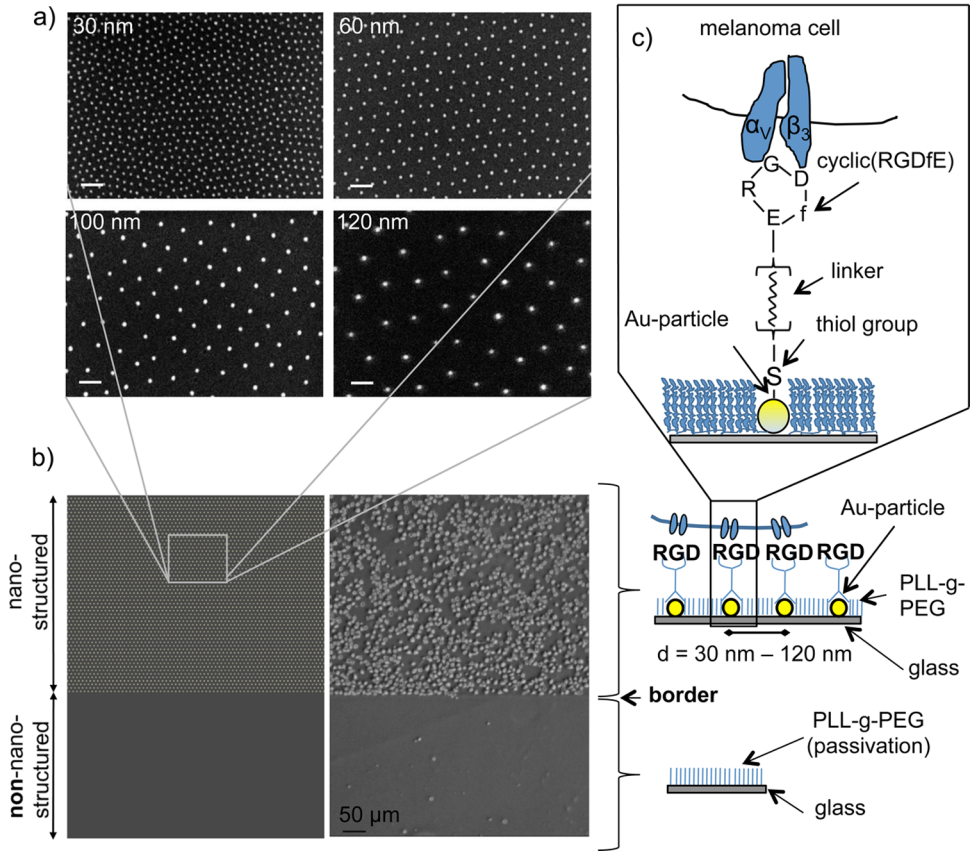

Figure 1. Nanostructured biofunctionalization with cyclic(RGDfE) facilitates melanoma cell interactions. (A) Scanning electron microscopy (SEM) images of gold (Au) nanoparticles with the indicated site densities; scale bar = 100 nm. (B) The border between the nanostructured and the non-nanostructured area creates a sharply demarcated line (left panel, simulated image). Melanoma cells (exemplified here with A375 cells) can bind only to the nanostructured area functionalized with cyclic(RGDfE) (right panel). (C) Schematic of melanoma cell $\alpha_V\beta_3$ integrin binding to cyclic(RGDfE). The thiol group of cyclic(RGDfE) is covalently linked to Au nanoparticles (simplified scheme; there are 100 to 1000 RGD molecules on a Au particle). A passivating polymer layer (PLL-*g*-PEG, poly L-lysine-grafted-polyethylenglycol) between the Au-NPs prevents nonspecific protein adsorption and cell binding.

densities relevant for integrin binding *in vivo* and in innovative *in vitro* models.[34,35] The Au-NPs served as anchor points for covalent binding of the thiol groups of cyclic(RGDfE), and the passivating PLL(20 kDa)-*g*-[3.5]-PEG(2 kDa) layer between the Au-NPs prevented nonspecific binding (Figure 1C).[36,37]

While functionalization of Au-NPs with proteins such as GPIbα[38] or *N*-cadherin[39] can be verified by fluorescent antibodies, RGD is not accessible to such direct detection. Therefore, successful RGD functionalization was demonstrated through an internal control of an unstructured part of the glass surface. As the entire surface underwent functionalization, the striking observance of the border by adhering cells, an internal control performed in each experiment, indicated that neither RGD nor cells bound nonspecifically to PLL-*g*-PEG (Figure 1B).

Cyclic(RGDfE) Nanostructures Specifically Facilitate $\alpha_V\beta_3$ Integrin Binding of Melanoma Cells. The next series of experiments addressed binding characteristics of four human melanoma lines[30−33] on cyclic(RGDfE), a peptide that is predicted to bind to $\alpha_V\beta_3$ and, to a lesser extent, to $\alpha_5\beta_1$ integrins.[28,29] As determined by flow cytometry, $\alpha_V\beta_3$ expression of the A375 and MeWo melanoma lines (MFI = 5596 and MFI = 4954, respectively, isotype background values subtracted) was 7- to 11-fold higher compared to the LOX or MelHO melanoma cells (MFI = 171 and MFI = 279, respectively, isotype values subtracted; Figure 2A). In contrast, $\alpha_5\beta_1$ was expressed at high levels by all four lines (MFI: A375 = 3869, LOX = 8923, MeWO = 3032, MelHo = 1624). When the four melanoma lines were analyzed for their ability to attach to nanoscopically presented cyclic(RGDfE), a striking correlation between cell

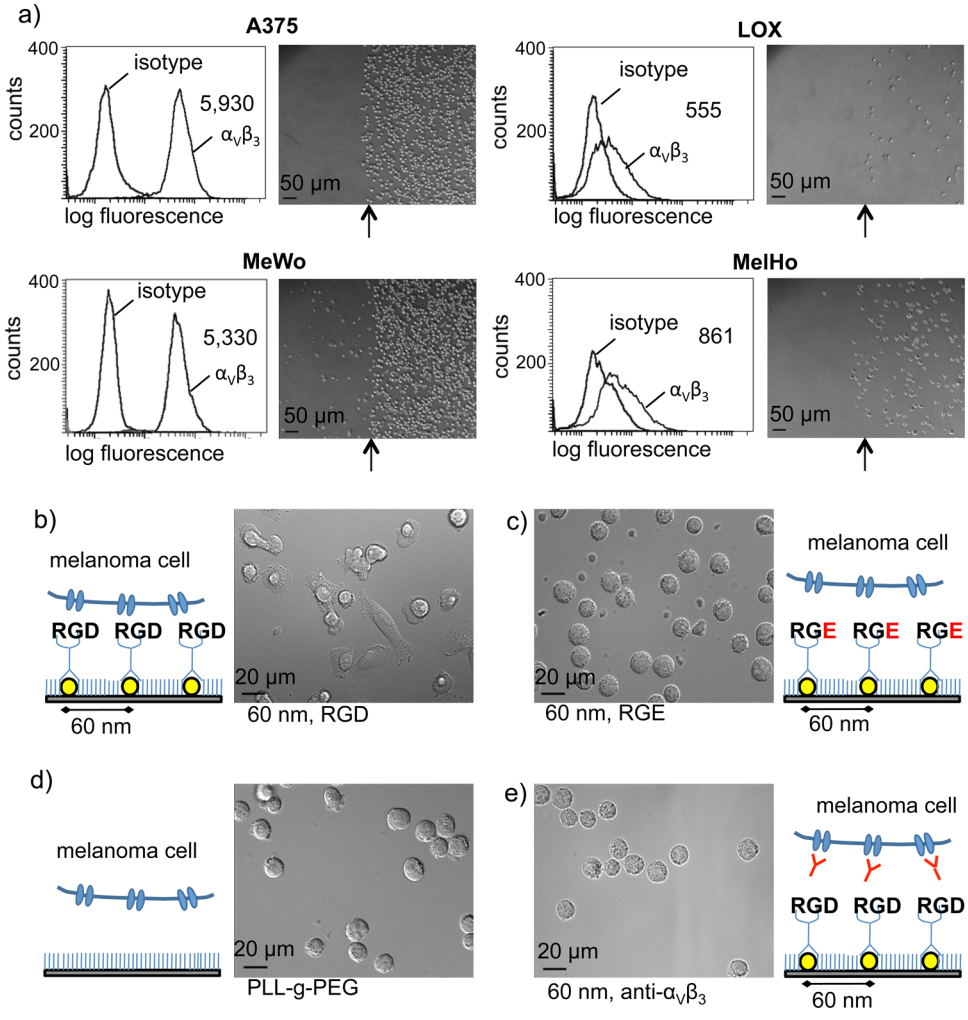

Figure 2. Human melanoma cells bind to nanoscopically presented cyclic(RGDfE) through the $\alpha_V\beta_3$ integrin. (A) Four human melanoma cell lines were screened for $\alpha_V\beta_3$ expression using flow cytometry. Two of them (A375 and MeWo) show very high $\alpha_V\beta_3$ expression; a dense layer of bound cells can be visualized bound to the nanostructured ligands beyond the borderline. In contrast, the MelHo and LOX lines show low expression of the $\alpha_V\beta_3$ integrin and bind only weakly to the nanostructured ligands. (B) Melanoma cells expressing the $\alpha_V\beta_3$ integrin readily spread on nanoscopically presented RGD, as visualized by DIC microscopy. (C−E) Melanoma cells do not bind to, but only float over, surfaces of nanoscopically presented RGE (arginine, glycine, and glutamic acid) (C), pegylated glass (D), or RGD surfaces incubated with $\alpha_V\beta_3$-blocking antibodies (E).

binding and $\alpha_V\beta_3$ expression became apparent (Figure 2A), whereas there was no correlation with $\alpha_5\beta_1$ expression.

A large series of control experiments was performed to support the specificity of the interaction between nanoscopic cyclic(RGDfE) and $\alpha_V\beta_3$ integrin on melanoma cells: First, functionalization of nanostructured surfaces with a similar amino acid sequence, that is, arginine, glycine, and glutamic acid (RGEfE), did not induce any cellular responses (Figure 2C). Likewise, melanoma cells failed to attach to PEGylated non-nanostructured areas (Figure 2D). Finally, function-blocking antibodies against the $\alpha_V\beta_3$ integrin completely abrogated melanoma cell attachment (Figure 2E). In contrast, untreated melanoma cells exposed to nanostructured (60 nm) surfaces functionalized with cyclic(RGDfE) efficiently attached and spread within 1 h (Figure 2B).

Further support for the pivotal role of $\alpha_V\beta_3$ for melanoma cell binding to nanostructured cyclic(RGDfE) came from serial subcultures of LOX, a melanoma line that showed weak binding and spreading due to its low expression of $\alpha_V\beta_3$ (Figure 2A). When individual LOX cells with high $\alpha_V\beta_3$ expression were separated from those with low expression by fluorescence-activated cell sorting (FACSort), the distinctly different expression levels were retained through several rounds of subculture and were even intensified when FACSort was repeated (Figure 3A). Of note, there were no differences or compensatory changes in other integrins between the subpopulations, thus providing a useful tool to further study $\alpha_V\beta_3$ functions while avoiding the imponderability of genetic manipulations.

While this rather stable phenotypic trait of LOX subpopulations was unexpected, it allowed us to compare otherwise identical melanoma cells (termed LOX_{parent} (MFI = 231), LOX_{high} (MFI = 495), LOX_{2xhigh} (MFI = 1030), and LOX_{low}, (MFI = 75), respectively; Figure 3B) regarding their interactions with nanostructured cyclic(RGDfE). Indeed, we observed a striking association of melanoma cell binding with high expression of $\alpha_V\beta_3$ (Figure 3C,D). While only few LOX_{low} cells (24 ± 16 per 10× field) adhered to and spread on nanostructured cyclic(RGDfE) (60 nm), LOX_{high} (98 ± 49) and LOX_{2xhigh} (284 ± 46) cells bound strongly, approaching the situation seen with A375 and MeWo cells, showing high $\alpha_V\beta_3$ expression. Thus, melanoma cell binding to and spreading on nanoscopically presented cyclic(RGDfE) was mediated preferentially, if not exclusively, by $\alpha_V\beta_3$.

Adherence to and Spreading on Nanoscopically Presented RGD Are Dichotomous Functions in Human Melanoma Cells. When different Au-NP surfaces (distances of 30, 60, 100, and 120 nm, corresponding to ligand site densities of 1145/μm^2, 349/μm^2, 132/μm^2, and 103/μm^2, respectively) functionalized with cyclic(RGDfE) were used for melanoma cell attachment, the average numbers or A375 cells per microscopic field were 380 cells (±82) on 30 nm, compared to 298 cells (±66) on 60 nm, 127 cells (±25) on 100 nm, and 82 (±22) cells on 120 nm, respectively. Attachment of the second high-expressing line, MeWo, was comparable to that of A375 cells (Figure 4A). Thus, binding of melanoma cells to cyclic(RGDfE) was linearly dependent on the ligand site densities (Figure 4A).

However, some surprising changes in cellular functions, which were not unidirectionally dependent on RGD density, became apparent when the spreading behavior of melanoma cells was assessed: An "intermediate" ligand site distance of 60 nm (density 349/μm^2) exerted the strongest facilitation of melanoma cell spreading, as analyzed at two time points (45 and 90 min, Figure 4B,C). In contrast, ligands presented more densely (distance 30 nm, density 1145/μm^2) or further apart (distance 120 nm, density 103/μm^2) triggered minimal or no spreading, despite strong adhesion on ligands 30 nm apart. Ligand distances of 100 nm clearly elicited some spreading, thus suggesting a threshold between 100 nm (density 132/μm^2) and 120 nm (density 103/μm^2) for both cell lines (Figure 4D exemplifies A375 spreading).

In detail, after 45 min, A375 melanoma cells had spread on nanoscopically presented RGD of 60 and 100 nm distances to sizes of 579 μm^2 (±89 μm^2) and 519 μm^2 (±49 μm^2), respectively. In contrast, ligand distances of 30 or 120 nm did not support cell spreading. After another 45 min, A375 melanoma cells clearly spread best on 60 nm surfaces with a significantly larger cell size compared to the other densities reaching 920 μm^2 (±101 μm^2) on average, in contrast to a cell size of 650 μm^2 (±49 μm^2) on 100 nm (Figure 4B, $p = 0.0003$ for 30 nm *vs* 60 nm, $p = 0.0006$ for 30 nm *vs* 100 nm, $p = 0.0006$ for 120 nm *vs* 100 nm, $p = 0.0006$ for 120 nm *vs* 60 nm, and $p = 0.015$ for 60 nm *vs* 100 nm). Minimal spreading of some cells was observed on 30 nm but not on 120 nm surfaces. Very similar results were obtained with MeWo cells (Figure 4B,C).

RGD Ligand Densities Determine Focal Contacts and Cytoskeletal Reorganization in Melanoma Cells. As cell spreading and polarization are governed by focal contacts and traction forces exerted by cytoskeletal fibers, vinculin (a linker between integrins and the cytoskeleton at focal contacts)[40] and F-actin (the predominant component of the cytoskeletal machinery) were visualized in A375 melanoma cells. In line with the conspicuous spreading behavior, focal contacts were readily detected on intermediate ligand distances of 60 nm (density 349/μm^2) and 100 nm (density 132/μm^2), respectively. In contrast, both 30 and 120 nm distances did not support focal contact formation, although few cells had begun to spread on 30 nm after 1.5 h (Figure 5A). In addition, F-actin stress fiber formation (visualized using phalloidin) could be detected only in melanoma cells spread on "intermediate" site densities

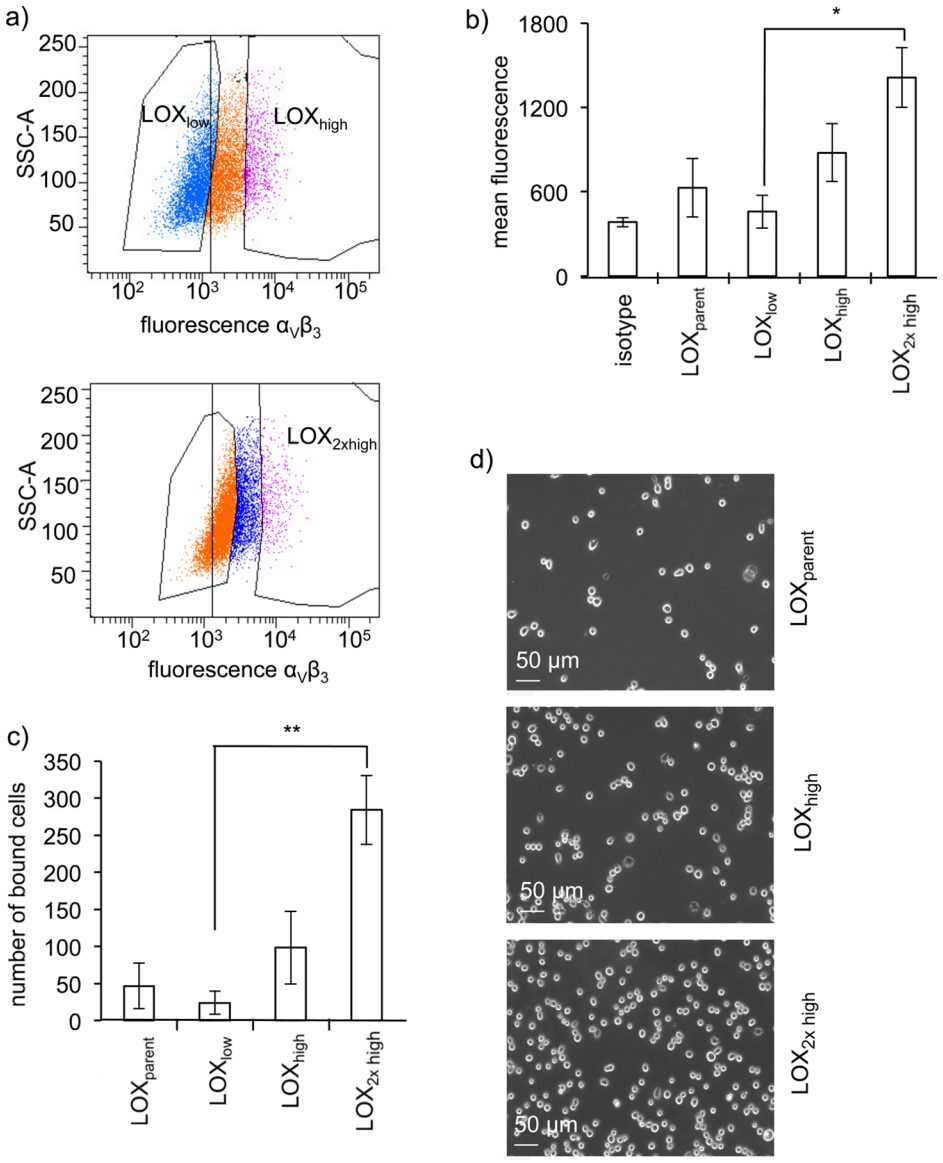

Figure 3. Subpopulations of LOX melanoma cells adhere to nanoscopically presented cyclic(RGDfE) in a strictly $\alpha_V\beta_3$-integrin-dependent manner. (A) LOX subpopulations with differential $\alpha_V\beta_3$ expression were isolated by fluorescence-activated cell sorting, resulting in LOX_{low} (blue) and LOX_{high} (purple) subpopulations (upper panel). The differential expression levels of $\alpha_V\beta_3$ were enhanced by serial sorting, yielding LOX_{2xhigh} cells (purple, lower panel). (B) Mean $\alpha_V\beta_3$ surface expression (±SEM) levels of the indicated subpopulations of LOX melanoma cells as measured by flow cytometry after two subsequent FACSort procedures ($n = 3$ independent experiments, $^*p = 0.01$ for $\alpha_V\beta_3$ expression of LOX_{low} *vs* LOX_{2xhigh}, analyzed with the two-sided Student's *t* test). (C) Mean attachment (±SD) per microscopic field of the indicated LOX subpopulations to nanoscopically presented cyclic(RGDfE) ($^{**}p = 0.0084$ for attachment of LOX_{low} *vs* LOX_{2xhigh}, analyzed with the two-sided-Student's *t* test). (D) Representative images of the indicated LOX subpopulations attached to cyclic(RGDfE) (60 nm).

of RGD (60 and 100 nm, respectively). However, 60 nm distances led to extensive stress fiber formation with robust fibers throughout the cell body, whereas 100 nm distances evoked only markedly smaller stress fibers located primarily at the cell margins (Figure 5A).

Some remarkable differences became apparent when focal contacts on ligand site distances of 60 and 100 nm, respectively, were analyzed in more detail: Cells from three independent experiments were evaluated morphometrically for size, number, and shape of their focal contacts using a standardized computer-based algorithm (lower cutoff at 10 pixels, corresponding to a diameter of ~0.63 μm). While the average numbers of focal contacts were similar in melanoma cells spreading on 60 nm surfaces and 100 nm surfaces, respectively, the variation between individual cells appeared to be markedly greater on the 100 nm surfaces as compared to the 60 nm surfaces (23 (±6) for 60 nm *vs* 20 (±15) for 100 nm; Figure 5B). Of particular note, however, focal contacts formed by melanoma cells spreading on 60 nm surfaces were significantly larger, reaching an average size of 1.10 μm^2 (±0.34 μm^2) compared to focal contacts on 100 nm surfaces, which reached an average size of only

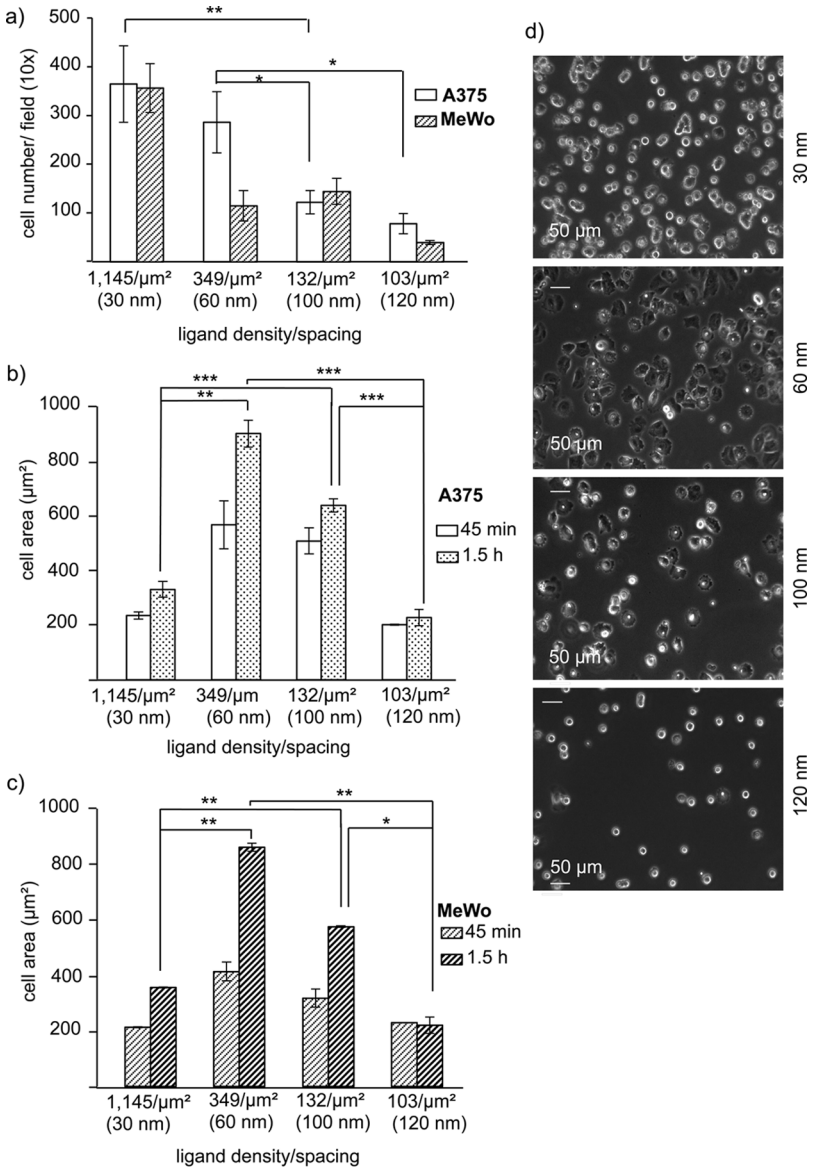

Figure 4. Ligand density controls melanoma cell spreading in a nonlinear fashion. (A) Melanoma cell binding is linearly dependent on ligand density. Mean cell numbers (±SD) of attached cells from 10 random microscopic 10× fields of three independent experiments are shown for A375 and MeWo, respectively. Adhesion of A375: $p = 0.004$ for 30 nm *vs* 100 nm, $p = 0.0202$ for 60 nm *vs* 100 nm, $p = 0.0186$ for 60 nm *vs* 120 nm. *$p < 0.05$; **$p < 0.01$. (B, C) Cell spreading as determined by measuring the cell surface areas is most pronounced on an intermediate ligand density, indicating a nonlinear correlation of cell surface and ligand site density. Analysis of A375 ($n = 4$ independent experiments) and MeWo melanoma cells ($n = 2$ experiments) on the different indicated ligand site densities of nanoscopically presented cyclic(RGDfE) was performed after 45 min and 1.5 h, respectively. Values shown represent the mean (±SEM) of 4 (A375) and 2 (MeWo) experiments. *$p < 0.05$; **$p < 0.01$; ***$p < 0.001$. After 1.5 h, the cell spreading area of melanoma cells on 60 nm surfaces is significantly larger compared to those of other ligand site densities (A375: $p = 0.003$ for 30 nm *vs* 60 nm, $p = 0.0006$ for 30 nm *vs* 100 nm, $p = 0.0006$ for 120 nm *vs* 100 nm, $p = 0.0006$ for 120 nm *vs* 60 nm, and $p = 0.015$ for 60 nm *vs* 100 nm; MeWo: $p = 0.0022$ for 30 nm *vs* 60 nm, $p = 0.0018$ for 30 nm *vs* 100 nm, $p = 0.018$ for 120 nm *vs* 100 nm, $p = 0.0067$ for 120 nm *vs* 60 nm, and $p = 0.0077$ for 60 nm *vs* 100 nm; global effect between 30, 60, 100, and 120 nm was assessed using one-way ANOVA; pairs were then analyzed with the two-sided Student's *t* test and subsequent Bonferroni adjustment). (D) Characteristic overview phase-contrast photomicrographs of A375 melanoma cells bound to the indicated RGD nanopatterns exemplifying linear dependency of numeric binding (see graph a) on RGD density, in contrast to a "bell-shaped" spreading behavior with a maximum at 60 nm ligand site distances.

0.50 μm^2 (±0.24 μm^2; $p < 0.0001$; Figure 5C). Thus, between 60 and 100 nm some critical regulations of focal contact formation and cytoskeletal reorganization occurred that created a "permissive" receptor–ligand interaction supporting cell spreading.

F-Actin-Dependent Cell Protrusions Are Governed by RGD Density. Given that maturation of focal contacts has been implicated in actin dynamics,[41] we further analyzed cytoskeletal functions of melanoma cells spread on 60 and 100 nm surfaces, respectively. The predominant patterns of F-actin-dependent cellular protrusions, *i.e.*, lamellipodia, filopodia, or a mixture of both (intermediate phenotype), were determined morphometrically: F-actin accumulation at the cells'

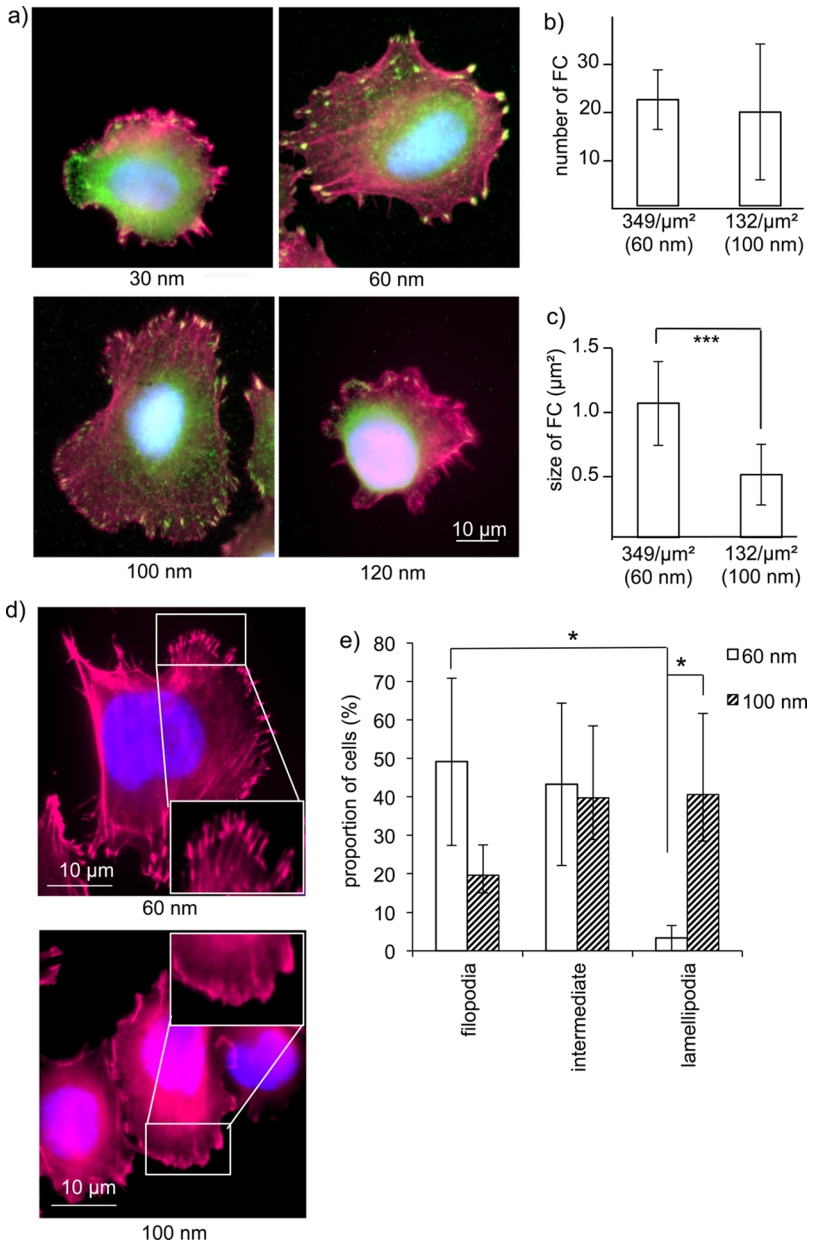

Figure 5. Formation of focal contacts and stress fibers in human melanoma cells is regulated by the density of nanoscopically presented RGD. (A) Focal contacts (FC) were visualized by antivinculin, and F-actin stress fibers were stained by phalloidin. Ligand site distances of 60 and 100 nm, respectively, support focal contact and stress fiber formation, in contrast to distances of 30 or 120 nm (n = 3 independent experiments). (B) Focal contacts of 10 representative cells each from 3 independent experiments on RGD site distances of 60 and 100 nm, respectively, were quantified using ImageJ. Values shown represent the mean (±SD). The number of focal contacts per cell on surfaces with 100 nm ligand site distances is markedly more variable compared to those on 60 nm ligand distances. (C) Focal contacts of A375 melanoma cells on 60 nm ligand site distances are significantly larger than those on 100 nm ligand site distances, ***p = 0.000 000 8 comparing 60 nm *vs* 100 nm, analyzed with the two-sided Student's t test. (D, E) The formation of cellular protrusions has been analyzed as a parameter of differential regulation of actin dynamics. On surfaces with 60 nm RGD ligand site distances, 50.8% of the cells (±20%) form filopodia, while only 3% of the cells (±3%) form lamellipodia (values shown represent the mean ± SD, *p = 0.025 for percentage number of cells forming filopodia *vs* lamellipodia on 60 nm, analzyed with the two-sided Student's t test). In contrast, lamellipodia formation is favored significantly on 100 nm (40.6% of the cells (±21%); *p = 0.0387 comparing the proportion of cells forming lamellipodia on 100 nm *vs* that on 60 nm, analyzed with the two-sided Student's t test).

edges without protrusions was defined as lamellipodia, whereas thin protrusions associated with stress fibers were defined as filopodia.

Indeed, some significant morphological differences became apparent: On 60 nm surfaces, 50.8% (±20%) of melanoma cells developed filopodia as their predominant cellular protrusions, while only 3.5% (±3%) formed lamellipodia, and 45.7% showed an intermediate phenotype. In sharp contrast, 40.6% (±21%) of the cells spread on 100 nm surfaces predominantly formed lamellipodia, whereas 19.6% (±8%) formed filopodia, and 39.8% exhibited both kinds of

protrusions (Figure 5D). These striking differences suggested that impairment of focal contact maturation (in melanoma cells spread on 100 nm surfaces) supported lamellipodia formation, whereas ligand site distances of 60 nm (density of 349/μm^2) facilitated the formation of full-fledged filopodia.

Low-Dose RGD Analogues "Permit" Melanoma Cell Spreading through Shifts of the Ligand Density Optimum. Our results revealed an optimum ligand site density for cell spreading, focal contact formation, and cytoskeletal reorganization (*i.e.*, functions implicated in metastasis formation and tumor progression) at 349/μm^2. We hypothesized that the underlying "permissive" receptor–ligand ratio could also be achieved experimentally through modulating the availability of surface receptors by solute ligands, thus mimicking the situation in patients treated with receptor-blocking drugs. Toward this end, melanoma cells on surfaces with 30 nm ligand site distances, *i.e.*, high-density conditions that did not by themselves support spreading and contact formation (Figure 3), were treated with nanomolar concentrations of solute RGD (ranging from 0.1 to 10.0 nM) for 20 min prior to adding the cells to the nanostructured surfaces (these concentrations were by order of magnitude below those inhibiting adhesion, which were approximately 200 nM; data not shown).

When melanoma cells were treated thus for 20 min, a marked shift of the optimum ligand site density occurred toward higher densities previously not able to support spreading and contact formation: After 45 min and 1.5 h, respectively, RGD concentrations of as low as 1.0 to 2.0 nM led to significantly enhanced spreading and contact formation of melanoma cells on cyclic(RGDfE) presented at a ligand site distance of 30 nm (density 1145/μm^2; Figure 6A,B). Indeed, compared to untreated melanoma cells (average cell size 216 μm^2 ($\pm$16 μm^2) after 45 min), melanoma cells increased their contact surface by approximately 75% following incubation with 2.0 nM solute RGD (average size 350 μm^2 ($\pm$80 μm^2), $p < 0.05$). When melanoma cells were treated with 10.0 nM of solute RGD, the "spreading boost" achieved by the lower RGD concentrations was completely abrogated (average size 216 μm^2 ($\pm$4 μm^2); Figure 6A). The alterations of melanoma spreading observed after 45 min were maintained in principle after 1.5 h (Figure 6A).

The next series of experiments addressed the question of whether this shift toward a "permissive" state of melanoma cell spreading on surfaces with 30 nm ligand site distances was accompanied by the according focal contact clustering and cytoskeletal reorganization. Indeed, while untreated melanoma cells did not show clustering of integrin $\alpha_V\beta_3$, an assembly step initiating focal contact formation,[42,43] this process was readily detectable once melanoma cells had been exposed to low-dose solute RGD prior to the contact to nanoscopically presented cyclic(RGDfE). Of note, the pattern of $\alpha_V\beta_3$ integrin clustering in low-dose RGD-treated melanoma cells on surfaces with ligand site distances of 30 nm (1145/μm^2) was similar to that seen with untreated melanoma cells spreading on surfaces with 3-fold lower ligand site distances (349/μm^2; Figure 6B,C). Likewise, F-actin stress fibers were induced by low-dose RGD in melanoma cells spreading on surfaces with 30 nm ligand distances, albeit somewhat less pronounced as compared to untreated melanoma cells spreading on 60 nm surfaces (Figure 6C).

Thus, low concentrations of solute RGD shifted melanoma cells into a "permissive state" that allowed tumor cell spread, focal contact formation, and cytoskeletal reorganization on ligand patterns they would otherwise not be able to spread on.

DISCUSSION

The RGD tripeptide is a well-characterized recognition motif for integrins interacting with ECM proteins.[28,44,45] Integrin specificity depends on the amino acids flanking RGD and the motif's configuration (experimentally: cyclic *vs* linear).[8,28,29] We used the cyclic pentapeptide cyclic(RGDfE) with high affinity for $\alpha_V\beta_3$, an integrin implicated in progression of melanoma, the most aggressive human skin cancer.[16,46]

Overcoming indiscriminate ligand immobilization, nanotechnology has greatly facilitated analyses of receptor–ligand interactions with a focus on biophysically relevant ECM characteristics such as ligand density, stiffness, or geometry.[47–49] Using block copolymer (micellar) nanolithography, our model enabled the tunable presentation of different ligand site densities through the hexagonal planar assembly of nanoparticles. The resulting nanostructured cyclic(RGDfE) ligand site densities spanned 1 order of magnitude. In contrast to previous studies with fibroblasts and osteoblasts[24,25] the ligand site densities of our system could be adjusted to densities of up to 1145/μm^2 (distances of 30 nm), a feature that is relevant in light of natural RGD spacings of 42 nm on fibrillar fibronectin[50] and approximately 30 nm on oncofetal fibronectin,[51] respectively.

However, the nanoscale distribution of binding motifs within the tumor microenvironment is difficult to determine, so the ligand site densities chosen in our study represent the best approximation to the *in vivo* situation discernible from currently available data. Especially melanoma cells can reorganize the ECM, *e.g.*, through MMP-mediated protein degradation or by attracting fibroblasts, thus actively modulating RGD binding site densities.[49,52]

Surprisingly and in striking contrast to adhesion (attachment), ligand site densities control melanoma cell spreading in a nonlinear mode of dependency. In two different melanoma lines with high $\alpha_V\beta_3$ expression, spreading was most pronounced on an intermediate ligand site density of 349 nanoparticles/μm^2 (lateral spacing of 60 nm). However, either increasing or decreasing the ligand site density abrogated full

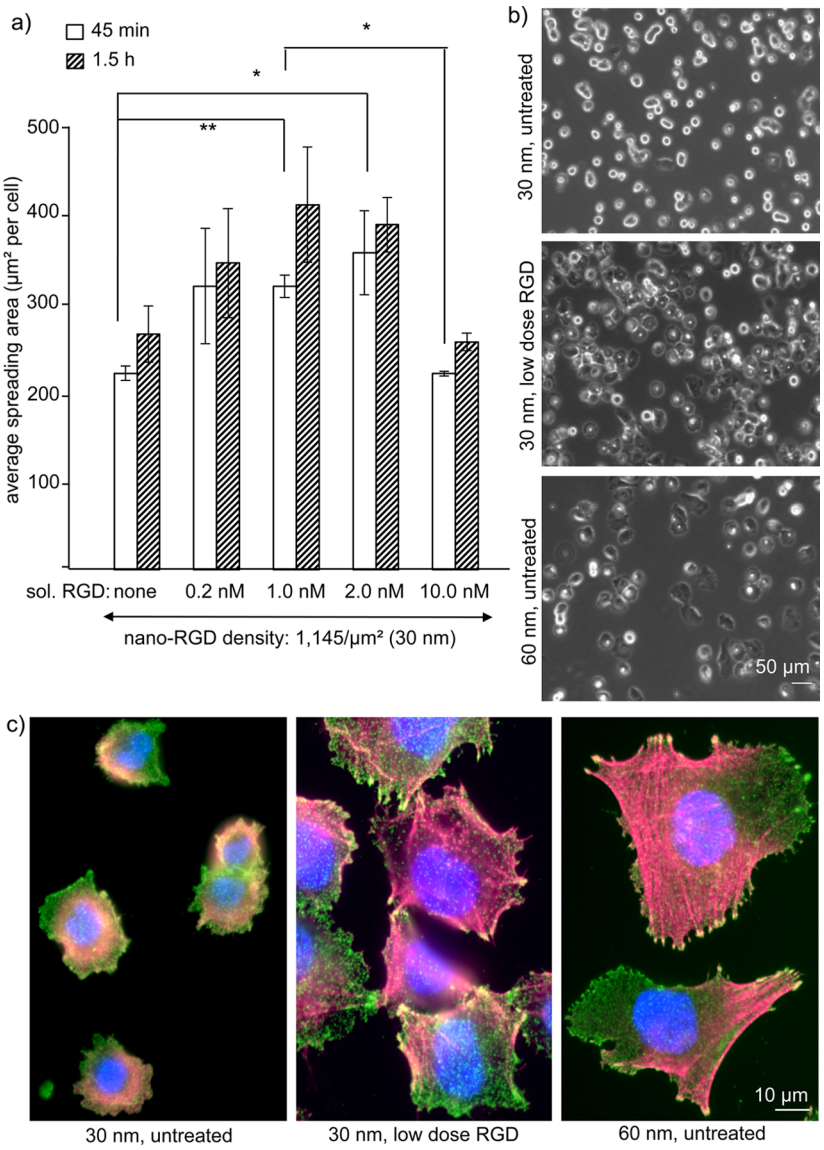

Figure 6. Low doses of solute RGD induce a "permissive" state of melanoma cells, allowing spreading and contact formation on surfaces with high ligand densities: (A) Spreading of 50 cells per condition was analyzed by digital morphometry. Values shown represent the mean of 4 independent experiments (±SEM; *$p < 0.05$, **$p < 0.01$). After 45 min (open bars), treatment with low doses of solvent RGD (1.0 or 2.0 nM) significantly enhances cell spreading on surfaces with 30 nm ligand site distances compared to untreated cells and cells treated with 10.0 nM of solute RGD ($p = 0.1842$ for "no treatment" *vs* 0.2 nM; $p = 0.0011$ for "no treatment" *vs* 1.0 nm; $p = 0.0209$ for "no treatment" *vs* 2.0 nM; $p = 0.3685$ for 10.0 vs 0.2 nM, $p = 0.0095$ for 10.0 vs 1 nM; all analyzed with the two-sided Student's *t* test). After 1.5 h (gray shaded bars), the differences were essentially sustained. (B) Representative photomicrographs of untreated A375 melanoma cells on surfaces with 30 nm ligand site distances, of low-dose-RGD-pretreated A375 melanoma cells on 30 nm surfaces, and of untreated A375 melanoma cells on 60 nm nanostructured surfaces were taken as indicated. (C) Corresponding immunofluorescence staining for integrin $\alpha_V\beta_3$ (green), F-actin (phalloidin, red), and DAPI (blue). Unlike ligand site distances of 30 nm (density 1145/μm^2), ligand site distances of 60 nm (right panel, ligand site density 349/μm^2) support integrin clustering associated with stress fiber formation. Treatment with solute RGD at a concentration of 1.0 nm restores the capacity of human melanoma cells to spread, form contacts, and establish stress fibers on a nanostructured surface with a cyclic(RGDfE) ligand site distance of 30 nm (middle panel).

cellular spreading. The critical threshold that determined a dramatic shift of melanoma cell functions appeared to lie between 60 and 100 nm. This notion was underscored by the tumor cells' ability to form well-developed filopodia along with large focal contacts and properly structured actin cytoskeletal lattices on 60 nm surfaces, while 100 nm surfaces produced smaller and irregular focal contacts, less well developed actin cytoskeletons, and fewer filopodia.

To interpret why melanoma cells spread optimally at a ligand site density of 349/μm^2, we can delineate several lines of explanation, which are not mutually exclusive: First, as demonstrated previously,[35,53] the formation of integrin clusters is an important prerequisite for cytoskeletal engagement and, subsequently, successful cell spreading.[54] Along this line, interspatial distances of 60 nm appear to be crucial for the formation of cluster units consisting of four integrins and

consecutive cell spreading.[35] Indeed, the relevance of 60 nm ligand site distances for optimal integrin clustering has been associated with the size of cytoplasmic proteins like talin, which itself has a size of 60 nm[55] and acts as a cross-linker during integrin aggregation.[35,43] It is conceivable that this mechanism contributed to the impaired accumulation of cytoplasmic proteins on surfaces of 30 nm ligand site spacing if we assume that lateral distribution of integrins is controlled by the respective interspatial distance of the opposing nanosurface.

Second, lateral movement of integrins is crucial for their successful clustering. Several studies have indicated that unligated integrins become recruited to focal adhesions,[56,57] a function that might be hampered at very dense extracellular RGD ligand presentations through rapid binding of available integrins and consecutive hindrance of their lateral mobility. It is, therefore, reasonable to assume that at nanostructured ligand site distances of 30 nm, which correspond to a high ligand site density of about 1145/μm^2 and (in contrast to conventional protein adsorption) feature an "ortho"-directed presentation of the binding motif, this lateral shift and the consecutive formation of integrin clusters become impaired.

Third, our immunofluorescence analyses showed large round focal contact patches of melanoma cells interacting on 60 nm ligand site distances, in contrast to significantly smaller and elongated focal patches on 100 nm surfaces. It is thought that focal contacts of $\geq$1.0 μm^2 represent mature "focal adhesions", which are associated with low mobility of the cells, whereas elongated and small patches of below 1.0 μm^2 are termed "focal complexes", which are associated with a more migratory and mobile phenotype.[40]

On the basis of the surprising existence of an optimal ligand density "permissive" for melanoma cell spreading, modulating the receptor–ligand ratio through suboptimal dosages of integrin-blocking solute RGD "shifted" melanoma cell functional states toward spreading and cytoskeletal reorganization. A certain increase of cell spreading over time may be influenced by very low levels of residual unbound RGD. It is intriguing to speculate that during antitumoral therapies *in vivo* with repeated administrations of drugs such as cilengitide,[14] trough concentrations of the compound could (repeatedly) shift tumor cell functions toward such a "permissive" state rather than inhibit their progression. This notion adds another level of complexity to potential responses of malignant tumors to targeted therapies. In clinical settings, suboptimal doses of a receptor-blocking compound may elicit unpredictable and unwanted effects, a notion that should give rise to more thorough evaluations of dosing intervals, pharmacodynamics, and pharmacokinetics. In our experimental system, it appears possible that during preincubation of melanoma cells with low-dose solute RGD some receptors were blocked and, thus, no longer accessible for surface-immobilized RGD. This reduction of interacting receptors may then lead to a net RGD–receptor interaction comparable to that seen on 60 or 100 nm surfaces. Given the short time that melanoma cells need to spread on RGD and an incubation time with solute RGD of 20 min, it appears likely that a considerable proportion of solute RGD was bound to melanoma cells before they settled onto the surfaces. Consequently, it is less likely that relevant amounts of unbound RGD with thiol residues interacted with the pegylation or with nonsaturated Au-NPs, which is a theoretical possibility. Besides, interaction of RGD with the pegylation on 30 nm surfaces would have produced an even higher ligand density and, consequently, further diminished melanoma cell spreading.

The shift of the "permissive" phenotype of melanoma cells is relevant to recent findings showing "paradoxical" growth enhancement of A375-melanoma tumors in mice upon treatment with low-dose RGD analogues, an effect that was attributed primarily to a pro-angiogenic activity.[14] Our study, by demonstrating a direct influence of low-dose RGD on melanoma cell spreading on given ligand patterns, now suggests an additional or alternative explanation, which would not have been possible without the use of nanotechnology.

CONCLUSIONS

Our results demonstrate that low nanomolar concentrations of RGD significantly enhanced melanoma spreading on RGD at interligand distances of 30 nm, *i.e.*, a ligand site density that is normally prohibitive for melanoma cell spreading. One can hypothesize that such "suboptimal" concentrations of integrin-directed antitumoral compounds also shift melanoma cells into "permissive" states *in vivo*. These situations, even if they occur only temporarily during dosing intervals, may suffice to facilitate melanoma cell spreading and metastasis. Indeed, RGD analogues such as cilengitide have short half-lives *in vivo* due to drug metabolism and serum degradation.[58–61] Consequently, low plasma levels are predicted to occur rapidly after drug application. Intriguingly, we have demonstrated the formation of integrin clusters associated with F-actin in melanoma cells treated with low nanomolar concentrations of solute RGD.

METHODS

Defined Nanoscale Ligand Presentation (Nanostructuring). Nanostructured surfaces were fabricated by using block copolymer (micellar) nanolithography.[25] In short, glass cover slides (24 × 24, No. 1, Carl Roth, Karsruhe, Germany) were cleaned in caroic acid (1 h, 1:3 H_2O_2 (30%)/H_2SO_4 (p.A., Merck, Darmstadt,

Germany). These glass slides were then sonicated four times for 5 min each and dried with N_2. Micellar solutions were prepared in a glove box (Braun, Garching, Germany) by dissolving the polystyrene−polyvinylpyridine-*block*-copolymers (Polysciences, Warrington, PA, USA) in toluene (Merck). The micelles' cores were then loaded with $HAuCl_4 \cdot 3H_2O$ (Sigma, St. Louis, MO, USA). The cleaned glass coverslips were dip-coated into the micelle solution. Organic parts of the micelles were removed by plasma treatment (10% H_2, 90% argon, 0.4 mbar, 150 W, TePla 100; PVA, Wettenberg, Germany). Gold nanoparticles were thus firmly bound to the glass surface.

We generated nanoscopically defined surfaces with a wide range of Au-NP spacings (mean distances between adjacent nanoparticle sites). The actual densities of each batch of nanosurfaces were determined precisely by scanning electron microscopy (SEM Ultra 55; Zeiss, Göttingen, Germany) and covered the range from 1145/μm^2 (corresponding to ligand site distances of 30 nm) to 103/μm^2 (ligand site distances of 120 nm), with several in-between densities as indicated in the text and figures. As micellar block copolymer nanolithography results in a quasi-hexagonal assembly of the nanoparticles, the ligand site density can also be approximated by applying the formula $\rho = 2/(d^2\sqrt{3})$.

Biofunctionalization of Nanostructured Surfaces. Nanostructured and UV-ozone-cleaned (UV-Ozone Cleaning System UVOH 150 LAB, FHR Anlagenbau, Ottendorf-Okrilla, Germany) glass surfaces (0.8 slm for 10 min) were incubated at pH 7.4 for 45 min in an aqueous solution containing 0.5 mg/mL PLL(20 kDa)-*g*-[3.5]-PEG(2 kDa) (SuSoS, Dübendorf, Switzerland) in 10 mM HEPES (4-(2-hydroxyethyl)piperazine-1-ethanesulfonic acid; Calbiochem, San Diego, CA, USA) on parafilm (American National Can, Chicago, IL, USA). This procedure reliably passivated the surface areas between the Au-NPs, thus preventing nonspecific cell binding in these areas. Afterward, the surfaces were inverted and washed in *aqua dest.* for 30 min. For functionalization, the surfaces were incubated with 10 μM cyclic RGDfE (cyclo(RGDfE), [PEG-5-linker (22 atoms)]3-CCC; from PSL, Heidelberg, Germany) or with 25 μM of the control peptide RGEfE (PSL) for 3 h on parafilm. In the text the short forms of RGD (for cyclo(RGDfE)) and RGE (for cyclo-(RGDfE)) are used. Both peptides contain a thiol group, which covalently binds to the Au nanoparticles. Surfaces were washed again with *aqua dest.* for 30 min and equilibrated in Dulbecco's minimal essential medium (DMEM) supplemented with 1% BSA (Roth) prior to the experiments.

Cell Culture and Cell Experiments. For cell experiments the nanostructured surfaces were inserted into 60 mm Petri dishes (Greiner Bioone, Kremsmünster, Austria). Four human melanoma lines, A375 (30), MeWo (31), LOX (32), and MelHO (33), were grown in DMEM supplemented with 10% fetal calf serum, 100 U/mL penicillin, and 100 mg/mL streptomycin (Gibco, Karsruhe, Germany).

Functionalized nanostructured surfaces with density-controlled-RGD presentation were washed and stored in *aqua dest.* for at least 30 min. During that time, melanoma cells were harvested using Accutase (PAA, Pasching, Austria), washed with PBS (PAA), and resuspended in "attachment-medium" (DMEM supplemented with 1% BSA (Roth) without FCS). Cells recovered for 20 min and were then allowed to settle onto the surfaces at a concentration of 200 000/mL for 30 min. Surfaces with bound melanoma cells were washed with PBS (Gibco) for 5 min in a standardized fashion. For analysis of cell attachment, bound cells were counted on 10 representative images (10×). For further spreading analysis, surfaces with bound melanoma cells were transferred into Petri dishes containing "spreading-medium" (DMEM with 5% FCS). Preliminary tests had shown that medium containing 5% FCS did not lead to nonspecific bindings.

For blocking experiments, suspended melanoma cells were incubated with an azide-free anti-$\alpha_v\beta_3$-antibody (15 μg/mL; clone LM609, Millipore, Billerica, MA, USA) at 37 °C for 20 min and then allowed to settle on the functionalized nanostructured surfaces. For enhancement of cell spreading, cells were pretreated for 20 min under gentle rocking using varying doses of RGD (0.2 to 10.0 nM, the same RGD used for functionalization of surfaces). Afterward, cells were allowed to spread on the nanosurfaces for 30 min, and then surfaces were washed for 5 min. After defined time intervals (specified in the Results Section) standardized overview photomicrographs (10× = 420 μm × 560 μm) were analyzed morphometrically using ImageJ software (http://rsb.info.nih.gov/ij/index.html).

Flow Cytometry and Fluorescence-Activated Cell Sorting. Melanoma cells (in their exponential growth phase) were harvested using Accutase (PAA), washed with PBS once, resuspended in PBS containing 5% human male AB-serum (Sigma), and incubated with 1 μg/mL of either anti-$\alpha_v\beta_3$ (clone LM609, Millipore), anti-α_5 (clone SAM-1, Beckman-Coulter, Brea, CA, USA), anti-β1 (clone 4B4LDC9LDH8, Beckman-Coulter), or an IgG1 isotype control (Zymed, Wien, Austria). Surface-bound primary antibodies were detected using 0.5 μL of Alexa Fluor 488-conjugated goat-derived anti-mouse IgG (H+L) as a secondary reagent. Analysis was performed using the FACS Canto II and the FACS Diva software (BD Biosciences, San Jose, CA, USA).

For cell sorting, 10 × 10^6 cells of the melanoma line LOX_{parent} were stained with an azide-free anti-$\alpha_v\beta_3$ (clone LM609, Millipore) antibody. In the first cell sorting process, 5% of LOX_{parent} cells with the highest $\alpha_v\beta_3$ expression and 55% with the weakest $\alpha_v\beta_3$ expression (termed LOX_{low}) were separated and cultivated. After several rounds of subculture the process was repeated with the original 5% (termed LOX_{high}), and again the 5% with the highest $\alpha_v\beta_3$ expression were collected and further cultured (termed LOX_{2high}).

Immunofluorescence and Differential Interference Contrast (DIC) Microscopy. Melanoma cells attached to the experimental nanostructured surfaces were washed for 10 min with PBS and fixed with 4% paraformaldehyde for 20 min. Blocking was performed with 5% FCS in PBS, followed by antivinculin (clone hVIN-1, Sigma) or anti-$\alpha_v\beta_3$ (clone LM609, Millipore) mAbs for 3 h at room temperature or at 4 °C overnight. After 3 washing steps in PBS, cells were incubated with Alexa Fluor 488-conjugated anti-mouse IgG $F(ab')_2$ (Cell Signaling, Danvers, MA, USA) for 1 h. F-Actin was then stained with phalloidin (PromoFluor-55; PromoCell, Heidelberg, Germany) for 30 min. Fluorescence mounting medium (Dako, Hamburg, Germany) containing 0.5 μg/mL DAPI (Sigma) resulted in nuclear staining.

Phase contrast and fluorescence microscopy were performed on an Axiovert 200 or an AxioImager M1 system (Zeiss). DIC microscopy was performed on an AxioImager microscope equipped with a 40× plan apochromat oil immersion objective (NA 1.4) with polarization filters (Zeiss).

Data Analysis and Statistical Analysis. All data are displayed as mean (±SD or ± SEM as indicated). In order to detect differences between the Au-NP spacings, a one-way ANOVA was performed to determine a possible global effect. If a global effect could be demonstrated, corresponding independent *t* tests were performed. Their global type I error rate was defined as 5%. Thereafter, they were adjusted using the Bonferroni procedure to control the level at 5%. *p*-Values of <0.05 were considered statistically significant. All statistical tests were two-sided. All statistical analyses were conducted using Excel and Statistica 10 software.

Conflict of Interest: The authors declare no competing financial interest.

Acknowledgment. We gratefully appreciate the preparation of the nanostructured surfaces by the technicians at the Max Planck Institute for Intelligent Systems (Stuttgart, Germany). We thank Joachim P. Spatz (Max Planck Institute for Intelligent Systems) for important intellectual input and critical proofreading of the manuscript. We also thank Y. Schön for organizing the preparation of nanosurfaces and subsequent quality control by scanning electron microscopy.

REFERENCES AND NOTES

1. Patel, S. P.; Lazar, A. J.; Papadopoulos, N. E.; Liu, P.; Infante, J. R.; Glass, M. R.; Vaughn, C. S.; LoRusso, P. M.; Cohen, R. B.; Davies, M. A.; *et al.* Clinical Responses to Selumetinib (AZD6244; ARRY-142886)-Based Combination Therapy Stratified by Gene Mutations in Patients with Metastatic Melanoma. *Cancer* **2013**, *119*, 799–805.

2. Finn, L.; Markovic, S. N.; Joseph, R. W. Therapy for Metastatic Melanoma: The Past, Present, and Future. *BMC Med.* **2012**, *10*, 23.
3. Desgrosellier, J. S.; Cheresh, D. A. Integrins in Cancer: Biological Implications and Therapeutic Opportunities. *Nat. Rev. Cancer* **2010**, *10*, 9–22.
4. Garmy-Susini, B.; Avraamides, C. J.; Schmid, M. C.; Foubert, P.; Ellies, L. G.; Barnes, L.; Feral, C.; Papayannopoulou, T.; Lowy, A.; Blair, S. L. Integrin Alpha4beta1 Signaling Is Required for Lymphangiogenesis and Tumor Metastasis. *Cancer Res.* **2010**, *70*, 3042–3051.
5. Lowell, C. A.; Mayadas, T. N. Overview: Studying Integrins *in Vivo*. *Methods Mol. Biol.* **2012**, *757*, 369–397.
6. Kuphal, S.; Bauer, R.; Bosserhoff, A. K. Integrin Signaling in Malignant Melanoma. *Cancer Metastasis Rev.* **2005**, *24*, 195–222.
7. Brooks, P. C.; Clark, R. A.; Cheresh, D. A. Requirement of Vascular Integrin AlphaVbeta3 for Angiogenesis. *Science* **1994**, *264*, 569–571.
8. Mas-Moruno, C.; Rechenmacher, F.; Kessler, H. Cilengitide: the First Anti-Angiogenic Small Molecule Drug Candidate Design, Synthesis and Clinical Evaluation. *Anticancer Agents Med. Chem.* **2010**, *10*, 753–768.
9. Nabors, L. B.; Mikkelsen, T.; Hegi, M. E.; Ye, X.; Batchelor, T.; Lesser, G.; Peereboom, D.; Rosenfeld, M. R.; Olsen, J.; Brem, S.; *et al*. A Safety Run-In and Randomized Phase 2 Study of Cilengitide Combined with Chemoradiation for Newly Diagnosed Glioblastoma (NABTT 0306). *Cancer* **2012**, *118*, 5601–5607.
10. O'Donnell, P. H.; Undevia, S. D.; Stadler, W. M.; Karrison, T. M.; Nicholas, M. K.; Janisch, L.; Ratain, M. J. A Phase I Study of Continuous Infusion Cilengitide in Patients with Solid Tumors. *Invest. New Drugs* **2012**, *30*, 604–610.
11. Tentori, L.; Dorio, A. S.; Muzi, A.; Lacal, P. M.; Ruffini, F.; Navarra, P.; Graziani, G. The Integrin Antagonist Cilengitide Increases the Antitumor Activity of Temozolomide against Malignant Melanoma. *Oncol. Rep.* **2008**, *19*, 1039–1043.
12. Aguzzi, M. S.; D'Arcangelo, D.; Giampietri, C.; Capogrossi, M. C.; Facchiano, A. RAM, an RGDS Analog, Exerts Potent Anti-Melanoma Effects *in Vitro* and *in Vivo*. *PLoS One* **2011**, *6*, e25352.
13. Kim, K. B.; Prieto, V.; Joseph, R. W.; Diwan, A. H.; Gallick, G. E.; Papadopoulos, N. E.; Bedikian, A. Y.; Camacho, L. H.; Hwu, P.; Ng, C. S. A Randomized Phase II Study of Cilengitide (EMD 121974) in Patients with Metastatic Melanoma. *Melanoma Res.* **2012**, *22*, 294–301.
14. Reynolds, A. R.; Hart, I. R.; Watson, A. R.; Welti, J. C.; Silva, R. G.; Robinson, S. D.; Da Violante, G.; Gourlaouen, M.; Salih, M.; Jones, M. C. Stimulation of Tumor Growth and Angiogenesis by Low Concentrations of RGD-Mimetic Integrin Inhibitors. *Nat. Med.* **2009**, *15*, 392–400.
15. Legler, D. F.; Wiedle, G.; Ross, F. P. Imhof BA. Superactivation of Integrin AlphaVbeta3 by Low Antagonist Concentrations. *J. Cell Sci.* **2001**, *114*, 1545–1553.
16. Seftor, R. E.; Seftor, E. A.; Hendrix, M. J. Molecular Role(s) for Integrins in Human Melanoma Invasion. *Cancer Metastasis Rev.* **1999**, *18*, 359–375.
17. Mould, A. P.; Askari, J. A.; Craig, S. E.; Garratt, A. N.; Clements, J.; Humphries, M. J. Integrin Alpha4beta1-Mediated Melanoma Cell Adhesion and Migration on Vascular Cell Adhesion Molecule-1 (VCAM-1) and the Alternatively Spliced IIICS Region of Fibronectin. *J. Biol. Chem.* **1994**, *269*, 27224–27230.
18. Prakash, M.; Kale, S.; Ghosh, I.; Kundu, G. C.; Datta, K. Hyaluronan-Binding Protein 1 (HABP1/p32/gC1qR) Induces Melanoma Cell Migration and Tumor Growth by NF-kappa B Dependent MMP-2 Activation through Integrin Alpha(v)-beta(3) Interaction. *Cell Signal.* **2011**, *23*, 1563–1577.
19. Maheshwari, G.; Wells, A.; Griffith, L. G.; Lauffenburger, D. A. Biophysical Integration of Effects of Epidermal Growth Factor and Fibronectin on Fibroblast Migration. *Biophys. J.* **1999**, *76*, 2814–2823.
20. Rajagopalan, P.; Marganski, W. A.; Brown, X. Q.; Wong, J. Y. Direct Comparison of the Spread Area, Contractility, and Migration of Balb/c 3T3 Fibroblasts Adhered to Fibronectin- and RGD-Modified Substrata. *Biophys. J.* **2004**, *87*, 2818–2827.
21. Shebanova, O.; Hammer, D. A. Biochemical and Mechanical Extracellular Matrix Properties Dictate Mammary Epithelial Cell Motility and Assembly. *Biotechnol. J.* **2012**, *7*, 397–408.
22. Gaudet, C.; Marganski, W. A.; Kim, S.; Brown, C. T.; Gunderia, V.; Dembo, M.; Wong, J. Y. Influence of Type I Collagen Surface Density on Fibroblast Spreading, Motility, and Contractility. *Biophys. J.* **2003**, *85*, 3329–3335.
23. Arnold, M.; Cavalcanti-Adam, E. A.; Glass, R.; Blummel, J.; Eck, W.; Kantlehner, M.; Kessler, H.; Spatz, J. P. Activation of Integrin Function by Nanopatterned Adhesive Interfaces. *ChemPhysChem* **2004**, *5*, 383–388.
24. Arnold, M.; Hirschfeld-Warneken, V. C.; Lohmuller, T.; Heil, P.; Blummel, J.; Cavalcanti-Adam, E. A.; Lopez-Garcia, M.; Walther, P.; Kessler, H.; Geiger, B.; *et al*. Induction of Cell Polarization and Migration by a Gradient of Nanoscale Variations in Adhesive Ligand Spacing. *Nano Lett.* **2008**, *8*, 2063–2069.
25. Cavalcanti-Adam, E. A.; Volberg, T.; Micoulet, A.; Kessler, H.; Geiger, B.; Spatz, J. P. Cell Spreading and Focal Adhesion Dynamics are Regulated by Spacing of Integrin Ligands. *Biophys. J.* **2007**, *92*, 2964–2974.
26. Huang, J.; Grater, S. V.; Corbellini, F.; Rinck, S.; Bock, E.; Kemkemer, R.; Kessler, H.; Ding, J.; Spatz, J. P. Impact of Order and Disorder in RGD Nanopatterns on Cell Adhesion. *Nano Lett.* **2009**, *9*, 1111–1116.
27. Kruss, S.; Erpenbeck, L.; Schön, M. P.; Spatz, J. P. Circular, Nanostructured and Biofunctionalized Hydrogel Microchannels for Dynamic Cell Adhesion Studies. *Lab Chip* **2012**, *12*, 3285–3289.
28. Hersel, U.; Dahmen, C.; Kessler, H. RGD Modified Polymers: Biomaterials for Stimulated Cell Adhesion and Beyond. *Biomaterials* **2003**, *24*, 4385–4415.
29. Thumshirn, G.; Hersel, U.; Goodman, S. L.; Kessler, H. Multimeric Cyclic RGD Peptides as Potential Tools for Tumor Targeting: Solid-Phase Peptide Synthesis and Chemoselective Oxime Ligation. *Chemistry* **2003**, *9*, 2717–2725.
30. Giard, D. J.; Aaronson, S. A.; Todaro, G. J.; Arnstein, P.; Kersey, J. H.; Dosik, H.; Parks, W. P. *In Vitro* Cultivation of Human Tumors: Establishment of Cell Lines Derived from a Series of Solid Tumors. *J. Natl. Cancer Inst.* **1973**, *51*, 1417–1423.
31. Bean, M. A.; Bloom, B. R.; Herberman, R. B.; Old, L. J.; Oettgen, H. F.; Klein, G.; Terry, W. D. Cell-Mediated Cytotoxicity for Bladder Carcinoma: Evaluation of a Workshop. *Cancer Res.* **1975**, *35*, 2902–2913.
32. Fodstad, O.; Hansen, C. T.; Cannon, G. B.; Statham, C. N.; Lichtenstein, G. R.; Boyd, M. R. Lack of Correlation between Natural Killer Activity and Tumor Growth Control in Nude Mice with Different Immune Defects. *Cancer Res.* **1984**, *44*, 4403–4408.
33. Brüggen, J.; Sorg, C. Detection of Phenotypic Differences on Human Malignant Melanoma Lines and their Variant Sublines with Monoclonal Antibodies. *Cancer Immunol Immnuother.* **1983**, *15*, 200–205.
34. Hak, S.; Helgesen, E.; Hektoen, H. H.; Huuse, E. M.; Jarzyna, P. A.; Mulder, W. J.; Haraldseth, O.; Davies Cde, L. The Effect of Nanoparticle Polyethylene Glycol Surface Density on Ligand-Directed Tumor Targeting Studied *in Vivo* by Dual Modality Imaging. *ACS Nano* **2012**, *6*, 5648–5658.
35. Schvartzman, M.; Palma, M.; Sable, J.; Abramson, J.; Hu, X.; Sheetz, M. P.; Wind, S. J. Nanolithographic Control of the Spatial Organization of Cellular Adhesion Receptors at the Single-Molecule Level. *Nano Lett.* **2011**, *11*, 1306–1312.
36. Heuberger, M.; Drobek, T.; Voros, J. About the Role of Water in Surface-Grafted Poly(ethylene glycol) Layers. *Langmuir* **2004**, *20*, 9445–9448.
37. Pasche, S.; Voros, J.; Griesser, H. J.; Spencer, N. D.; Textor, M. Effects of Ionic Strength and Surface Charge on Protein Adsorption at PEGylated Surfaces. *J. Phys. Chem. B* **2005**, *109*, 17545–17552.

38. Kruss, S.; Erpenbeck, L.; Amschler, K.; Mundinger, T. A.; Boehm, H.; Helms, H. J.; Friede, T.; Andrews, R. K.; Schön, M. P.; Spatz, J. P. Adhesion Maturation of Neutrophils on Nanoscopically Presented Platelet Glycoprotein Ibalpha. *ACS Nano* **2013**, *7*, 9984–9996.
39. Wolfram, T.; Belz, F.; Schoen, T.; Spatz, J. P. Site-Specific Presentation of Single Recombinant Proteins in Defined Nanoarrays. *Biointerphases* **2007**, *2*, 44–48.
40. Deakin, N. O.; Ballestrem, C.; Turner, C. E. Paxillin and Hic-5 Interaction with Vinculin Is Differentially Regulated by Rac1 and RhoA. *PLoS One* **2012**, *7*, e37990.
41. Lutz, R.; Pataky, K.; Gadhari, N.; Marelli, M.; Brugger, J.; Chiquet, M. Nano-Stenciled RGD-Gold Patterns that Inhibit Focal Contact Maturation Induce Lamellipodia Formation in Fibroblasts. *PLoS One* **2011**, *6*, e25459.
42. Zaidel-Bar, R.; Cohen, M.; Addadi, L.; Geiger, B. Hierarchical Assembly of Cell-Matrix Adhesion Complexes. *Biochem. Soc. Trans.* **2004**, *32*, 416–420.
43. Selhuber-Unkel, C.; Lopez-Garcia, M.; Kessler, H.; Spatz, J. P. Cooperativity in Adhesion Cluster Formation During Initial Cell Adhesion. *Biophys. J.* **2008**, *95*, 5424–5431.
44. Smith, J. W.; Cheresh, D. A. Integrin (AlphaVbeta3)-Ligand Interaction. Identification of a Heterodimeric RGD Binding Site on the Vitronectin Receptor. *J. Biol. Chem.* **1990**, *265*, 2168–2172.
45. Cheng, Y. F.; Clyman, R. I.; Enenstein, J.; Waleh, N.; Pytela, R.; Kramer, R. H. The Integrin Complex AlphaVbeta3 Participates in the Adhesion of Microvascular Endothelial Cells to Fibronectin. *Exp. Cell Res.* **1991**, *194*, 69–77.
46. Desgrosellier, J. S.; Barnes, L. A.; Shields, D. J.; Huang, M.; Lau, S. K.; Prevost, N.; Tarin, D.; Shattil, S. J.; Cheresh, D. A. An Integrin AlphaVbeta3-c-Src Oncogenic Unit Promotes Anchorage-Independence and Tumor Progression. *Nat. Med.* **2009**, *15*, 1163–1169.
47. Lohmüller, T.; Aydin, D.; Schwieder, M.; Morhard, C.; Louban, I.; Pacholski, C.; Spatz, J. P. Nanopatterning by Block Copolymer Micelle Nanolithography and Bioinspired Applications. *Biointerphases* **2011**, *6*, MR1–12.
48. Pla-Roca, M.; Fernandez, J. G.; Mills, C. A.; Martinez, E.; Samitier, J. Micro/Nanopatterning of Proteins *via* Contact Printing Using High Aspect Ratio PMMA Stamps and Nanoimprint Apparatus. *Langmuir* **2007**, *23*, 8614–8618.
49. Jiao, Y.; Feng, X.; Zhan, Y.; Wang, R.; Zheng, S.; Liu, W.; Zeng, X. Matrix Metalloproteinase-2 Promotes AlphaVbeta3 Integrin-Mediated Adhesion and Migration of Human Melanoma Cells by Cleaving Fibronectin. *PLoS One* **2012**, *7*, e41591.
50. Dzamba, B. J.; Peters, D. M. Arrangement of Cellular Fibronectin in Noncollagenous Fibrils in Human Fibroblast Cultures. *J. Cell Sci.* **1991**, *100*, 605–612.
51. Schiefner, A.; Gebauer, M.; Skerra, A. Extra-Domain B in Oncofetal Fibronectin Structurally Promotes Fibrillar Head-to-Tail Dimerization of Extracellular Matrix Protein. *J. Biol. Chem.* **2012**, *287*, 17578–17588.
52. Hofmann, U. B.; Westphal, J. R.; Van Muijen, G. N.; Ruiter, D. J. Matrix Metalloproteinases in Human Melanoma. *J. Invest Dermatol.* **2000**, *115*, 337–344.
53. Yu, C. H.; Luo, W.; Sheetz, M. P. Spatial-Temporal Reorganization of Activated Integrins. *Cell Adhes. Migr.* **2012**, *6*, 280–284.
54. Maheshwari, G.; Brown, G.; Lauffenburger, D. A.; Wells, A.; Griffith, L. G. Cell Adhesion and Motility Depend on Nanoscale RGD Clustering. *J. Cell Sci.* **2000**, *113*, 1677–1686.
55. Critchley, D. R. Focal Adhesions - the Cytoskeletal Connection. *Curr. Opin. Cell Biol.* **2000**, *12*, 133–139.
56. Hirata, H.; Ohki, K.; Miyata, H. Mobility of Integrin Alpha5-beta1Measured on the Isolated Ventral Membranes of Human Skin Fibroblasts. *Biochim. Biophys. Acta* **2005**, *1723*, 100–105.
57. Ballestrem, C.; Hinz, B.; Imhof, B. A.; Wehrle-Haller, B. Marching at the Front and Dragging Behind: Differential AlphaVbeta3-Integrin Turnover Regulates Focal Adhesion Behavior. *J. Cell Biol.* **2001**, *155*, 1319–1332.
58. Eskens, F. A.; Dumez, H.; Hoekstra, R.; Perschl, A.; Brindley, C.; Bottcher, S.; Wynendaele, W.; Drevs, J.; Verweij, J.; van Oosterom, A. T. Phase I and Pharmacokinetic Study of Continuous Twice Weekly Intravenous Administration of Cilengitide (EMD 121974), a Novel Inhibitor of the Integrins AlphaVbeta3 and Alphavbeta5 in Patients with Advanced Solid Tumours. *Eur. J. Cancer* **2003**, *39*, 917–926.
59. Hariharan, S.; Gustafson, D.; Holden, S.; McConkey, D.; Davis, D.; Morrow, M.; Basche, M.; Gore, L.; Zang, C.; O'Bryant, C. L.; *et al.* Assessment of the Biological and Pharmacological Effects of the AlphaVbeta3 and AlphaVbeta5 Integrin Receptor Antagonist, Cilengitide (EMD 121974), in Patients with Advanced Solid Tumors. *Ann. Oncol.* **2007**, *18*, 1400–1407.
60. Pflugfelder, A.; Kochs, C.; Blum, A.; Capellaro, M.; Czeschik, C.; Dettenborn, T.; Dill, D.; Dippel, E.; Eigentler, T.; Feyer, P.; *et al.* S3-Guideline "Diagnosis, Therapy and Follow-Up of Melanoma". *J. Dtsch. Dermatol. Ges.* **2013**, *11*, 563–602.
61. Zimmer, L.; Vaubel, J.; Livingstone, E.; Schadendorf, D. Side Effects of Systemic Oncological Therapies in Dermatology. *J. Dtsch. Dermatol. Ges.* **2012**, *10*, 475–486.